Chemical Science

ROYAL SOCIETY OF CHEMISTRY

EDGE ARTICLE

View Article Online
View Journal

Cite this: DOI: 10.1039/d6sc01508e

All publication charges for this article have been paid for by the Royal Society of Chemistry

Asymmetric electronic modulation in bridged Cu–O_2–Ni dual-atom catalysts promoting CO_2 electroreduction

Xue Bai,[a] Liyuan Xiao,[a] Xiaoqin Xu,[a] Anaer Husile,[a] Fuquan Bai,[b] Lina Li*[c] and Jingqi Guan*[a]

Atomically precise heteronuclear dual-site configuration provides an effective strategy to overcome the intrinsic activity and selectivity limitations of single-atom systems in the electrochemical CO_2 reduction reaction (CO_2RR). Here, we introduce an oxygen-bridged Cu–O_2–Ni dual-atom catalyst supported on N-doped graphene (Cu–O_2–Ni-NG) through an ultrafast Joule-heating process. This rapid treatment enables precise formation of heteronuclear Cu–Ni pairs while preventing metal migration, yielding well-defined Cu–O_2–Ni active sites. Comprehensive characterization studies verify atomic dimer dispersion and strong electronic coupling between the two metal centers through a stable O-bridge. In the CO_2RR, Cu–O_2–Ni-NG exhibits exceptional CO selectivity (>95%), high catalytic activity, and outstanding operational stability, outperforming the corresponding monometallic controls. *Operando* Raman spectroscopy reveals potential-dependent evolution of *CO and carbonate species, consistent with a CO-dominant reaction pathway. Density functional theory calculations further show that the O-bridged Cu–O_2–Ni geometry optimizes *COOH adsorption, enhances interfacial charge transfer, and synergistically tunes the d-band centers of both metals, thereby lowering the rate-determining energy barrier while effectively suppressing the competing hydrogen evolution reaction. This work establishes oxygen-bridged heteronuclear dimers as a highly efficient platform for the CO_2RR and highlights the critical role of bridge-atom engineering in the rational design of next-generation dual-site electrocatalysts.

Received 22nd February 2026
Accepted 9th April 2026

DOI: 10.1039/d6sc01508e

rsc.li/chemical-science

Introduction

The rising atmospheric concentration of CO_2 and its detrimental impact on the climate and ecosystems have underscored the urgency of transformative carbon management strategies.[1,2] Carbon capture and utilization (CCU) offers a particularly attractive route, as it not only mitigates CO_2 emissions but also enables the conversion of this greenhouse gas into value-added fuels and chemicals, thereby establishing a circular carbon economy.[3,4] Among the available approaches, the CO_2RR powered by renewable electricity stands out as a viable pathway toward carbon neutrality. Within the product spectrum of the CO_2RR, CO is especially appealing as a critical feedstock for Fischer–Tropsch synthesis and other C_1 chemistry, which underpins large-scale production of hydrocarbons and alcohols.[5] Yet, the kinetic inertness of CO_2, the competitive hydrogen evolution reaction (HER), and the difficulty of designing catalysts that simultaneously deliver high activity, selectivity, and stability remain formidable challenges.[6–8]

Single-atom catalysts (SACs) have emerged as a powerful paradigm to tackle these issues. By maximizing atomic utilization and offering uniform coordination environments, SACs exhibit excellent selectivity toward CO.[9] However, their catalytic performance is fundamentally constrained by the linear scaling relation between *COOH formation and *CO desorption, preventing the concurrent realization of low overpotentials, industrially relevant current densities, and robust durability. In addition, the intrinsically isolated nature of SACs limits the diversity of reaction pathways that can be accessed, which poses difficulties when multistep proton-electron transfer reactions are required. These limitations highlight the necessity of going beyond single-site design toward catalytic motifs capable of cooperative interactions.[10]

To break the intrinsic limitations of SACs, dual-atom catalysts (DACs) have attracted growing interest. By integrating two adjacent metal centers, DACs introduce cooperative effects inaccessible to single-atom systems.[11] The two atoms can play complementary roles in the catalytic cycle—for example, one site activates CO_2 while the other facilitates proton or electron transfer—thereby decoupling scaling relations and enhancing

[a]Institute of Physical Chemistry, National Demonstration Center for Experimental Chemistry Education, College of Chemistry, Jilin University, 2519 Jiefang Road, Changchun, 130021, P. R. China. E-mail: guanjq@jlu.edu.cn
[b]Laboratory of Theoretical and Computational Chemistry, Institute of Theoretical Chemistry, College of Chemistry, Changchun, 130023, P. R. China
[c]Shanghai Synchrotron Radiation Facility, Shanghai Advanced Research Institute, Shanghai, 201204, P. R. China. E-mail: lilina@sinap.ac.cn

overall kinetics.[12,13] Furthermore, heteronuclear DACs offer additional tunability, as the asymmetry between dissimilar metals allows for fine-tuned electronic structures and tailored adsorption energetics. Within this framework, CuNi DACs stand out as a representative system because of the complementary functionality of Cu and Ni centers. Ni atoms tend to promote CO_2 activation and stabilization of COOH intermediates, while Cu atoms excel in water dissociation and proton delivery.[14] Previous studies have shown that CuNi DACs coordinated by nitrogen or sulfur atoms can deliver high CO selectivity, with the bridging atom exerting a decisive influence on electronic redistribution. For instance, N-bridged Cu–N–Ni structures strengthen COOH adsorption *via* strong metal–ligand coupling,[15] whereas S-bridged Cu–S–Ni motifs facilitate intermetallic charge transfer, accelerating CO_2 activation.[16] These findings highlight that the identity of the bridging atom is not a passive structural element but a key determinant of catalytic behavior. Recent progress in Cu-based CO_2RR catalysts has demonstrated that strategies such as bimetallic site construction, alloying and valence state stabilization can effectively modulate electronic structures and catalytic performance, highlighting the potential of atomically precise dual-atom configurations as a powerful platform for further optimization.[17–20] In this regard, oxygen-bridged configurations offer an intriguing yet largely unexplored alternative. O bridges possess intermediate electronegativity and high chemical robustness, potentially providing a distinct balance of charge redistribution and stability compared with N or S counterparts. This unique characteristic makes oxygen-bridged Cu–O_2–Ni sites a promising platform for advancing CO_2 electroreduction. Despite their conceptual appeal, the controlled synthesis of oxygen-bridged DACs remains highly challenging because conventional pyrolysis routes lack precision and often lead to nanoparticle aggregation. This underscores the importance of developing rapid and controllable fabrication strategies that can lock metal atoms into desired coordination motifs while preserving the conductive carbon support.

Here, we introduce an oxygen-bridged Cu–O_2–Ni dual-atom catalyst (Cu–O_2–Ni-DAC) supported on graphene oxide, synthesized *via* an ultrafast Joule heating strategy. In this process, a CuNi bimetallic precursor is immobilized on graphene oxide and rapidly transformed within milliseconds, driving precise atomic fixation into Cu–O_2–Ni moieties while retaining the conductivity and structural integrity of the carbon scaffold. High-angle annular dark field scanning transmission electron microscopy (HAADF-STEM) and X-ray absorption spectroscopy (XAS) confirm the presence of atomically dispersed Cu–O_2–Ni sites, validating the success of this design. The Cu–O_2–Ni-DAC delivers outstanding CO_2RR performance, with CO FE above 90% across a wide potential range and excellent operational durability. *Operando* spectroscopy combined with density functional theory (DFT) calculations reveal that the oxygen bridge enhances electronic communication between Cu and Ni, lowers the barrier for *COOH formation, and facilitates *CO desorption. This cooperative mechanism effectively decouples the scaling relation between these key steps, enabling high activity alongside superior selectivity. These considerations motivated us to explore oxygen bridges as structural motifs for dual-site catalysis. In the Cu–O_2–Ni-DAC, the O atom serves as both a stabilizer and an electronic mediator between adjacent metal centers. Beyond advancing the CuNi system, this study highlights bridge-atom engineering as a generalizable principle for rationally designing next-generation DACs for sustainable CO_2 conversion. More broadly, this approach demonstrates how bridge-atom engineering, when combined with ultrafast synthesis strategies, can unlock previously inaccessible coordination environments, paving the way for the rational design of next-generation DACs tailored for sustainable CO_2 conversion.

Experimental methods

Synthesis of the [L(Cu–O_2–Ni)] precursor

The ligand H_2L was synthesized *via* a 2 : 1 condensation of 3-methoxysalicylaldehyde and ethylenediamine in methanol. For the preparation of the mononuclear complex [LCu(H_2O)], an aqueous solution of $Cu(OAc)_2 \cdot H_2O$ was added dropwise to a vigorously stirred suspension of H_2L in methanol. This resulted in the immediate formation of a green precipitate. The mixture was stirred for an additional 30 minutes, after which the solid product was isolated by filtration. The heterobinuclear complex [L(Cu–O_2–Ni)] was subsequently obtained by adding solid $Ni(NO_3)_2 \cdot 6H_2O$ to a methanolic suspension of [LCu(H_2O)], inducing a color change to green. Following 30 minutes of stirring, the solution was filtered. Green crystals suitable for single-crystal X-ray diffraction were grown by the slow diffusion of diethyl ether into the filtrate over a period of three days. The obtained crystals were collected by filtration, washed with a methanol/diethyl ether mixture, and subjected to recrystallization.

Synthesis of Cu–O_2–Ni-NG, Cu–N_2–Ni-NG, Cu-NG and Ni-NG

A homogeneous suspension was first prepared by ultrasonically dispersing 100 mg of graphene oxide (GO) and 4.83 mg of the heterobinuclear complex [L(Cu–O_2–Ni)] in 50 mL of deionized ethanol for 30 minutes. After removing the solvent *via* rotary evaporation, the precursor complex became anchored onto the GO sheets, primarily through electrostatic interactions and coordination with oxygen-containing functional groups on the GO surface. The resulting composite was then rapidly pyrolyzed under an N_2 atmosphere using a joule-heating-based ultrafast thermal processing system ($U = 30$ V, $I = 150$ A, $t \approx 200$ ms) with an estimated instantaneous temperature of ~1500 K, yielding the nitrogen-doped graphene-supported material, denoted as Cu–O_2–Ni-NG. For comparative purposes, Cu–N_2–Ni-NG was synthesized by pyrolysis of [L(Cu–O_2–Ni)]/GO under an NH_3 atmosphere. Cu-NG and Ni-NG were synthesized analogously by replacing the binuclear precursor with equivalent mononuclear copper and nickel complexes, respectively, followed by identical NH_3 pyrolysis conditions.

Results and discussion

Synthesis and characterization

Fig. 1a illustrates the synthetic protocol for constructing oxygen-bridged Cu–Ni dual-atom sites on graphene (Cu–O_2–Ni-NG). A

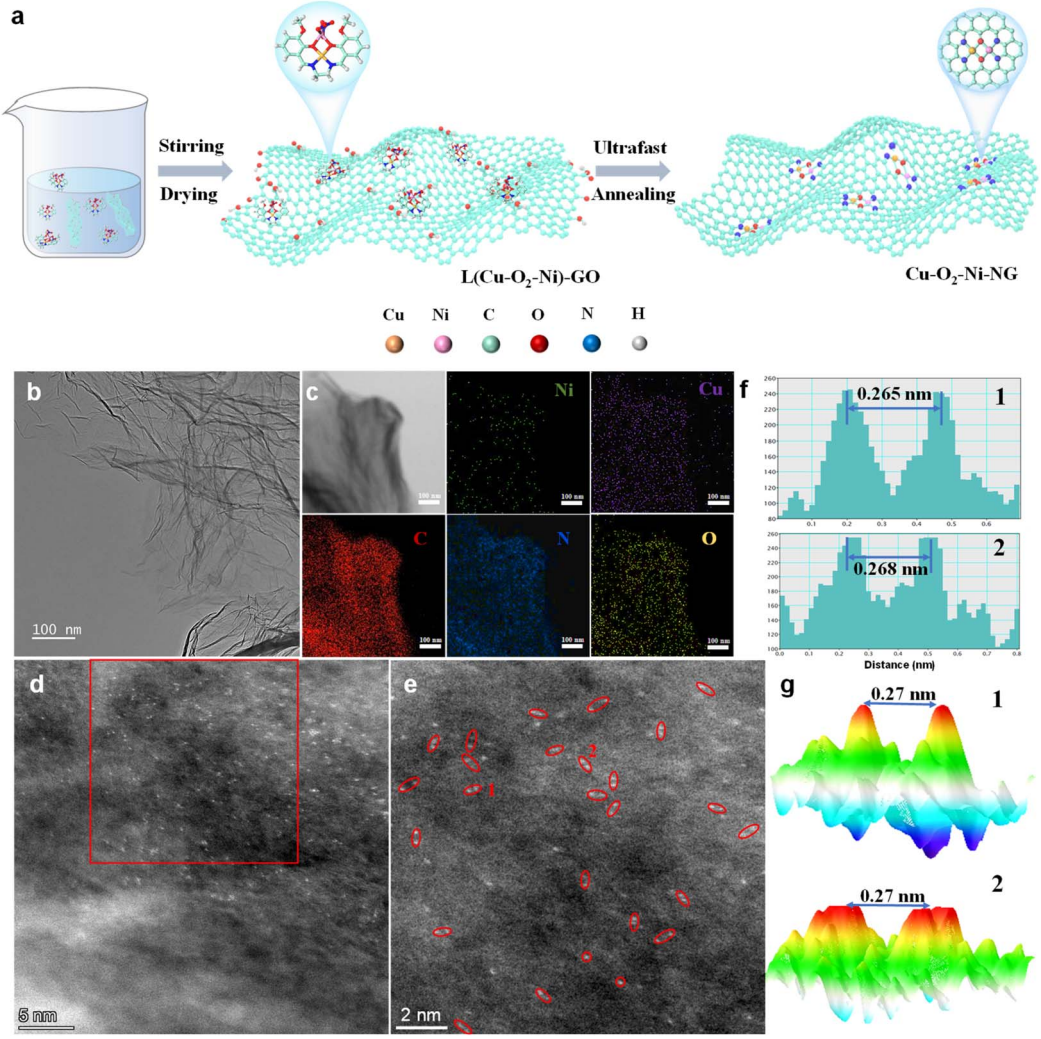

Fig. 1 (a) Schematic diagram of preparation of Cu–O_2–Ni-NG. (b) HRTEM image, (c) elemental mapping and (d and e) HAADF-STEM images of Cu–O_2–Ni-NG. (f) Intensity distribution. (g) 3D model of the Cu and Ni dual-atom sites in (e).

bimetallic CuNi precursor complex was first prepared through a recrystallization method, where Cu and Ni ions were coordinated with oxygen-containing ligands to pre-establish a Cu–O_2–Ni structural unit.[21] The successful formation of this precursor was verified using simulated XRD patterns (Fig. S1), confirming the presence of the oxygen-bridged heteronuclear moiety. The precursor was subsequently immobilized onto graphene oxide (GO) *via* electrostatic interaction, followed by freeze-drying to afford a uniform CuNi-GO composite. This intermediate was then subjected to ultrafast Joule heating, during which the instantaneous high temperature enabled rapid fixation of Cu and Ni atoms into oxygen-bridged dual sites, while simultaneously reducing GO into conductive graphene. The millisecond heating process effectively suppressed metal migration and aggregation, ensuring an atomically dispersed Cu–O_2–Ni configuration. For comparison, single-atom Cu-NG and Ni-NG catalysts were synthesized using the corresponding monometallic precursors under identical conditions.

Transmission electron microscopy (TEM) and high-resolution TEM (HRTEM) images of Cu–O_2–Ni-NG reveal that the catalyst exhibits a typical crumpled nanosheet morphology, characteristic of the reduced graphene framework, without observable metallic nanoparticles or aggregated domains (Fig. 1b). This sheet-like structure provides abundant exposed surface area and facilitates the homogeneous distribution of active sites. Elemental mapping obtained from energy-dispersive X-ray spectroscopy (EDS) clearly shows that Cu, Ni, O, and C are uniformly distributed across the entire graphene matrix (Fig. 1c), confirming the effective incorporation of both metal species. The atomic dispersion of the metal centers was further verified by aberration-corrected high-angle annular dark-field scanning transmission electron microscopy (AC-HAADF-STEM), in which a large number of adjacent bright dots are observed and highlighted (Fig. 1d and e). These features correspond to closely spaced Cu and Ni atoms anchored on the graphene support. The line profile analysis demonstrates that the distance between the two neighboring atoms is approximately 0.27 nm (Fig. 1f and g), consistent with the formation of a stable oxygen-bridged heteronuclear Cu–Ni dual-atom configuration. These results provide direct evidence

for the successful atomic-level construction of Cu–O_2–Ni active sites on the graphene substrate.

The crystalline structure of Cu–O_2–Ni-NG was examined by X-ray diffraction (XRD). As presented in Fig. S2, the diffraction pattern shows two broad peaks centered at approximately 25° and 44°, corresponding to the (002) and (101) planes of graphitic carbon. No diffraction signals associated with Cu, Ni, or their oxides and carbides are observed, suggesting that the metal species are atomically dispersed on the graphene substrate rather than forming crystalline particles.[22] X-ray photoelectron spectroscopy (XPS) was employed to probe the chemical states and electronic interactions within the catalysts (Fig. S3a). The N 1s spectrum of Cu–O_2–Ni-NG shows a pronounced M–N coordination peak, indicating strong bonding between metal centers and nitrogen functionalities. Compared with Cu-NG and Ni-NG, Cu–O_2–Ni-NG exhibits a higher fraction of metal-N species, suggesting the successful incorporation of both Cu and Ni atoms into the nitrogen coordination environment (Fig. S3b). In the Cu 2p region (Fig. S3c), the characteristic peak at 933.6 eV is assigned to Cu(II), without detectable contributions from Cu(I) or Cu(0). This peak exhibits a positive shift relative to Cu-NG, reflecting electronic redistribution and possible charge transfer from Cu to Ni.[14] Similarly, the Ni $2p_{3/2}$ peaks at 855.1 eV show a negative shift compared with Ni-NG (Fig. S3d), further confirming the electron interaction between Cu and Ni centers. In the O 1s region (Fig. S3e), a dominant peak at 531.7 eV is attributed to metal–O coordination, indicating the presence of bridging oxygen atoms between Cu and Ni. These oxygen bridges further mediate charge redistribution and stabilize dual-site configurations, ultimately tuning the electronic structure to enhance CO_2 reduction kinetics.

To gain atomic-level insight into the local coordination environment and electronic structure of the active sites, XAS measurements were carried out at both Cu and Ni K-edges. Compared with the XPS analysis, XAS provides element-specific information with higher sensitivity, enabling precise determination of oxidation states and coordination configurations. As shown in Fig. 2a, the Cu K-edge XANES spectrum of Cu–O_2–Ni-NG exhibits an absorption edge positioned between those of Cu foil and CuO, but slightly shifts to lower energies compared with Cu-NG, indicating an increase in electron density around the Cu center. This negative shift suggests that the introduction of Ni and the bridging oxygen enables partial electron back-donation to Cu, thereby lowering its effective oxidation state. A similar behavior is observed at the Ni K-edge (Fig. 2b), where the absorption edge of Cu–O_2–Ni-NG also exhibits a slight negative shift relative to Ni-NG, suggesting that Ni experiences an increase in local electron density. The simultaneous leftward shifts of both Cu and Ni edges provide direct evidence of electronic redistribution between the two metal centers *via* the O bridge, reflecting strong electronic coupling within the heteronuclear Cu–O_2–Ni coordination environment.[23] This observation aligns well with the XPS

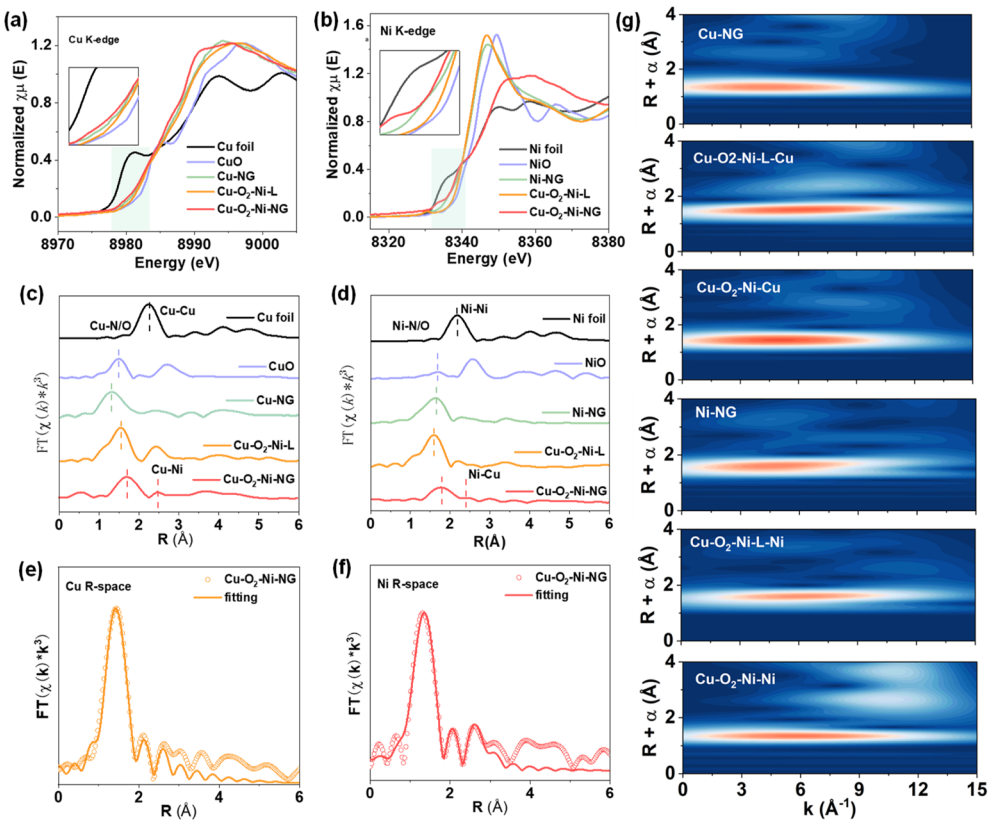

Fig. 2 (a) Cu K-edge XANES spectra of Cu foil, CuO, Cu-NG, Cu–O_2–Ni-L and Cu–O_2–Ni-NG samples. (b) Ni K-edge XANES spectra of Ni foil, NiO, Ni-NG, Cu–O_2–Ni-L and Cu–O_2–Ni-NG samples. (c) FT-EXAFS spectra of the Cu k-edge. (d) FT-EXAFS spectra of the Ni K-edge. (e and f) FT-EXAFS of the *R*-space fitting curve for Cu–O_2–Ni-NG. (g) WT–EXAFS plots.

analysis, further corroborating the existence of charge transfer between Cu and Ni mediated by the bridging oxygen atoms.

The corresponding Fourier-transformed EXAFS spectra (Fig. 2c and d) offer direct structural evidence of the local coordination environment. A distinct peak located at 1.5–1.9 Å is attributed to Cu–N/O and Ni–N/O coordination in the first shell. At the Cu K-edge, the main peak position is progressively shifted toward higher *R* values from Cu-NG to Cu–O_2–Ni-L and further to Cu–O_2–Ni-NG, reflecting the gradual modulation of the local coordination structure upon introducing Ni.[24] A similar rightward shift is also observed at the Ni K-edge for Cu–O_2–Ni-NG compared with Ni-NG and Cu–O_2–Ni-L, suggesting electronic and structural rearrangements around Ni centers during dual-site construction. In addition to the first-shell feature, a secondary scattering peak emerges at approximately 2.3–2.7 Å, corresponding to Cu–Ni interactions. The presence of this well-resolved second-shell signal verifies the formation of bimetallic Cu–Ni sites rather than isolated monometallic centers.[25] Compared with the monometallic counterparts (Cu-NG and Ni-NG), the second-shell peak of Cu–O_2–Ni-NG displays a slight shift to higher *R*, indicating a more ordered Cu–Ni coordination environment. In contrast, relative to the molecular precursor Cu–O_2–Ni-L, the peak position at the Cu K-edge remains nearly slightly shifted, whereas a more pronounced shift is observed at the Ni K-edge, highlighting the asymmetric structural evolution around the two metal centers. These observations collectively demonstrate that well-defined Cu–Ni dual sites are formed, accompanied by subtle yet discernible structural reconstruction compared with both monometallic references and the precursor.

To obtain quantitative structural parameters, EXAFS fitting was carried out (Fig. 2e, f and Table S1). The fitting results reveal that each Cu center is coordinated to approximately 3.2 N/O atoms, with a bond length of ~1.85 Å, and one Ni atom at ~2.59 Å. Similarly, the Ni center is coordinated to N/O at ~1.95 Å and Cu at ~2.67 Å. Such a configuration indicates that Cu and Ni atoms are bridged through oxygen species, forming a stable dual-site structure that enables charge delocalization and enhanced electronic interaction.

Wavelet transform (WT)–EXAFS analysis further validates these findings (Fig. 2g). The Cu K-edge WT contour map displays a strong intensity maximum at approximately 6.0 $Å^{-1}$, corresponding to Cu–N/O coordination. A second, weaker feature is observed at higher k-values, attributable to Cu–Ni scattering. No Cu–Cu signal is detected compared with Cu foil, confirming that Cu remains atomically dispersed rather than aggregated into metallic clusters. The Ni K-edge WT contour exhibits a similar pattern, reinforcing the dual-site structure conclusion. These observations collectively demonstrate that the local structure of Cu–O_2–Ni-NG is dominated by well-defined Cu–Ni dual sites with synergistically modulated electronic states, which are expected to play a crucial role in catalytic performance.[26]

CO_2RR performance

The electrocatalytic CO_2 reduction performance of the as-prepared catalysts was systematically evaluated in CO_2-saturated 1 M KOH electrolyte. As shown in Fig. 3a, linear sweep voltammetry (LSV) curves reveal that Cu–O_2–Ni-NG exhibits a much

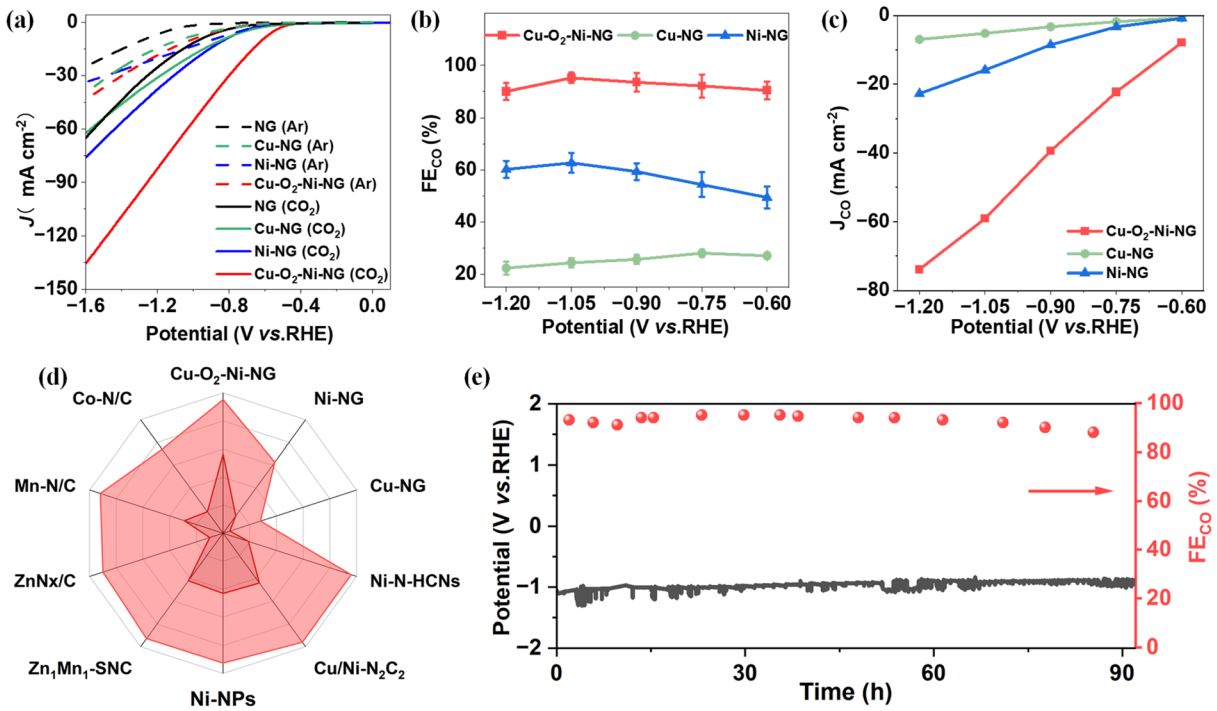

Fig. 3 (a) LSV curves of NG, Cu-NG, Ni-NG and Cu–O_2–Ni-NG obtained in CO_2-saturated 1 M KOH. (b) FE_{CO} at different potentials on Cu-NG, Ni-NG and Cu–O_2–Ni-NG. (c) The CO partial current densities of Cu-NG, Ni-NG and Cu–O_2–Ni-NG. (d) The comparison of FEs and current density of Cu–O_2–Ni-NG with those of other reported catalysts at −1.0 V *vs.* RHE. (e) Stability test of Cu–O_2–Ni-NG at a current density of 50 mA cm^{-2}.

higher current density than NG, Cu-NG and Ni-NG across the entire potential range, demonstrating its superior catalytic activity. Correspondingly, the faradaic efficiency toward CO (FE_{CO}) of Cu–O_2–Ni-NG reaches a maximum of 95.2% at −1.05 V *vs.* RHE (Fig. 3b, S4 and Table S2), which is notably higher than those of the monometallic counterparts. The partial current density for CO production (J_{CO}) (Fig. 3c) also shows a sharp increase, indicating an intrinsically more efficient reaction pathway facilitated by the dual-atom structure. The turnover frequency (TOF) for CO production at −1.05 V is 0.59 s^{-1} on Cu–O_2–Ni-NG (Table S3), which is approximately 5-fold and 2.5-fold higher than those of Cu-NG (0.11 s^{-1}) and Ni-NG (0.24 s^{-1}), respectively, confirming the superior intrinsic activity of the oxygen-bridged dual-atom sites. To further validate the critical role of the oxygen bridge, a control catalyst with a proposed nitrogen-bridged Cu–Ni configuration (Cu–N_2–Ni-NG) was synthesized under an NH_3 atmosphere. Cu–N_2–Ni-NG achieves a maximum CO faradaic efficiency of 86.3% at −0.9 V *vs.* RHE, which is significantly lower than that of Cu–O_2–Ni-NG (Table S4), highlighting the unique contribution of the oxygen bridge to the enhanced catalytic performance. To benchmark its performance, FE_{CO} of Cu–O_2–Ni-NG is compared with those of previously reported state-of-the-art catalysts (Fig. 3d and Table S5). Remarkably, Cu–O_2–Ni-NG outperforms most reported catalysts, exhibiting FE_{CO} exceeding 95%, which is among the best values reported to date for Cu/Ni-based catalysts. Meanwhile, the current density is also significantly greater than that of the other reported catalysts. This superior activity can be attributed to the synergistic electronic coupling between Cu and Ni centers mediated by oxygen bridges, which promotes CO_2 activation and intermediate stabilization.

To further probe the reaction kinetics, Tafel slope analysis was conducted (Fig. S5). Cu–O_2–Ni-NG displays a significantly lower Tafel slope than Cu-NG and Ni-NG, suggesting accelerated CO_2RR kinetics and reduced energy barriers. This kinetic enhancement is consistent with the optimized electronic structure of the dual-site configuration. Electrochemical impedance spectroscopy (EIS) further corroborates this conclusion (Fig. S6). Cu–O_2–Ni-NG exhibits the smallest semicircle radius in the Nyquist plot, indicating the lowest charge-transfer resistance among all samples, which facilitates fast electron transport during electrocatalysis. To evaluate the density of active sites, electrochemical surface area (ECSA) was determined based on the double-layer capacitance (C_{dl}) in the non-faradaic region (Fig. S7 and S8). The C_{dl} of Cu–O_2–Ni-NG is significantly higher than that of Cu-NG and Ni-NG, indicating a higher density of electrochemically accessible active sites, which correlates well with its enhanced catalytic current. Finally, durability tests were carried out at a constant potential of −1.05 V *vs.* RHE (Fig. 3e). Cu–O_2–Ni-NG retains stable current output and CO selectivity over 90 hours of continuous operation, confirming its excellent structural stability and operational durability under practical working conditions.

Mechanistic elucidation

To gain insight into the dynamic behavior of the active sites during the CO_2RR, *operando* Raman spectroscopy was first employed to track the evolution of surface species at applied potentials (Fig. S9). As the potential was swept from 0 to −1.2 V *vs.* RHE, a distinct band emerged at 1073 cm^{-1}, corresponding to the vibrational signature of adsorbed carbonate intermediates,[27–29] indicating efficient CO_2 adsorption and activation under cathodic conditions. Additionally, a clear peak at 2089 cm^{-1} was detected, which can be assigned to the ν(C≡O) stretching mode of adsorbed *CO intermediates.[30,31] The presence of these two characteristic features confirms the formation and stabilization of key intermediates along the CO pathway, consistent with the high CO selectivity observed for Cu–O_2–Ni-NG. To further elucidate the structural evolution of the catalyst during operation, post-reaction XPS measurement was conducted (Fig. S10). A new component appears at 933.0 eV in the Cu $2p_{3/2}$ region after the CO_2RR, corresponding to partially reduced Cu^+/Cu^0 species.[14] This suggests that Cu undergoes partial reduction during catalysis, likely associated with its participation in CO_2 activation and intermediate stabilization. In contrast, the Ni 2p spectrum shows no discernible changes relative to the pristine sample, and Ni remains predominantly in the Ni^{2+} state. The preserved oxidation state of Ni indicates that the Ni centers retain their structural integrity throughout the CO_2RR, highlighting their robustness and sustained catalytic functionality. Furthermore, the O 1s spectrum reveals a dominant peak at 532.2 eV, corresponding to the metal–O bond of the Cu–O_2–Ni bridge, with no evidence of oxygen species transformation, confirming the chemical stability of the oxygen bridge. Together, the *operando* spectroscopic observations and post-reaction surface analysis reveal a cooperative catalytic mechanism in which Cu actively engages in dynamic electron transfer during CO_2 activation, while Ni retains a stable oxidation state, ensuring persistent active-site stability under reaction conditions.

To further probe the structural robustness and coordination stability of the Cu–O_2–Ni dual sites under electrochemical operating conditions, post-reaction XAS spectroscopy was performed at both the Cu and Ni K-edges (Fig. 4 and Table S6). As shown in the Cu K-edge XANES spectra (Fig. 4a), the overall spectral profile of Cu–O_2–Ni-NG remains essentially subtle changes after the CO_2RR, with a slight shift of the absorption edge toward lower energies. This subtle shift is consistent with the partial reduction of Cu observed in the post-reaction XPS analysis, yet the preservation of the main-edge features confirms that the local coordination geometry around Cu is largely retained.[32] A similar trend is observed at the Ni K-edge (Fig. 4b), where the pre- and post-reaction spectra nearly overlap, indicating that the Ni centers retain their oxidation state and coordination structure throughout the reaction.

The FT-EXAFS spectra further corroborate these observations. In the Cu K-edge EXAFS (Fig. 4c), both the Cu–N/O first-shell peak and the Cu–Ni scattering peak exhibit a leftward shift after the reaction, suggesting minimal perturbation of the local bonding environment.[33] The Ni K-edge EXAFS (Fig. 4d) shows a comparable overall profile, while a rightward shift of the main scattering features is observed after the reaction, further validating the structural stability of the bimetallic configuration. Consistently, WT–EXAFS analysis (Fig. 4e)

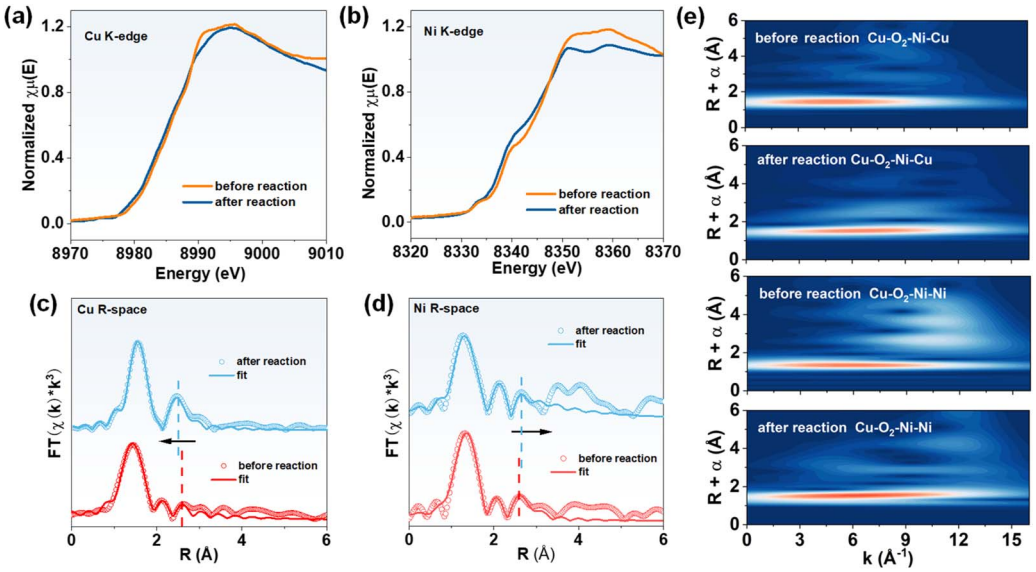

Fig. 4 (a) Cu K-edge and (b) Ni K-edge XANES spectra before and after the reaction of Cu–O_2–Ni-NG samples. (c) FT-EXAFS spectra of the Cu K-edge and (d) Ni K-edge. (e) WT–EXAFS plots.

reveals nearly identical wavelet intensity distributions before and after the reaction for both Cu and Ni edges, demonstrating that no new scattering paths emerge and that the dual-metal coordination framework remains intact. Taken together, the post-reaction XAS results confirm that the Cu–O_2–Ni moiety preserves its bimetallic coordination and electronic structure after the CO_2RR, which is further supported by post-reaction TEM analysis showing no obvious morphological change (Fig. S11). These findings, in combination with *operando* Raman and XPS analyses, establish that Cu participates dynamically in intermediate activation, while Ni retains structural stability, enabling a cooperative and durable catalytic mechanism.

To gain deeper insights into the reaction mechanism and the role of the coordination environment in Cu–O_2–Ni-NG, density functional theory (DFT) calculations were performed using six structural models: Cu–O_2–Ni-NG, Cu–N_2–Ni-NG, Cu–O–Ni-NG, CuNi-NG, Cu-NG, and Ni-NG (Fig. S12). The optimized adsorption configurations provide a detailed picture of the reaction pathway for CO_2 reduction (Fig. 5a and S13–S17). As shown in Fig. 5a, the CO_2 molecule initially adopts a side-on adsorption configuration at the Cu–Ni dual-metal center, followed by proton-electron coupling to form the *COOH intermediate. The *COOH species tilts slightly toward the Ni center, yet both Cu and Ni atoms jointly stabilize the intermediate through cooperative interactions. Subsequent protonation and cleavage of *COOH lead to *CO formation, which eventually desorbs to yield gaseous CO. The free-energy profiles of all models were calculated to elucidate the energetics of each elementary step (Fig. 5b). For every model, the conversion of *CO_2 to *COOH is endergonic and represents the rate-determining step (RDS) of the CO_2RR.[10] Among the tested configurations, Cu–O_2–Ni-NG requires the lowest energy barrier (1.29 eV) for *COOH formation, significantly lower than that required by the nitrogen-bridged bimetallic structures and mononuclear analogues. This result indicates that the oxygen-bridged dual-atom configuration facilitates CO formation more efficiently than its N-bridged counterparts or single-atom counterparts.

Density of states (DOS) analysis further clarifies the electronic effects induced by different bridging environments (Fig. 5c).[34] The d-band centers of the monometallic Cu-NG, and Ni-NG sites are located at −2.58 and −2.19 eV, respectively. By contrast, the dual-metal configurations show markedly shifted d-band centers: −2.24 eV for Cu–O_2–Ni-NG and −2.89 eV for Cu–N_2–Ni-NG. As optimal catalytic performance requires balanced adsorption strength for small-molecule intermediates, the moderated d-band position of the O-bridged Cu–O_2–Ni-NG model suggests an improved ability to regulate both adsorption and desorption processes. This electronic tuning capability explains the superior catalytic activity of the O-bridged dual-atom sites.

Because accelerated CO_2 activation requires efficient charge transfer, we further analyzed the differential charge density and Bader charge distributions. Graphene functions as an electron reservoir, continuously delivering electrons through the dual-metal center to drive CO_2 activation.[35] Upon *COOH adsorption, electron accumulation occurs predominantly on the carbon atom and the carbonyl oxygen within the *COOH intermediate, generated through d-orbital donation from the Cu and Ni centers (Fig. 5d). This electron enrichment induces a bent geometry in *COOH, a widely recognized feature associated with effective CO_2 activation.[36] Remarkably, the O-bridged Cu–O_2–Ni-NG model exhibits a charge transfer of 0.273 $|e|$ to the COOH intermediate, significantly higher than that of the N-bridged Cu–N_2–Ni-NG and mononuclear structures (Fig. S18), confirming stronger electronic coupling mediated by the oxygen bridge. In addition to promoting the CO_2RR, Cu–N_2–Ni-NG also exhibits a higher reaction barrier toward the competing HER compared with N-bridged dimers and SACs

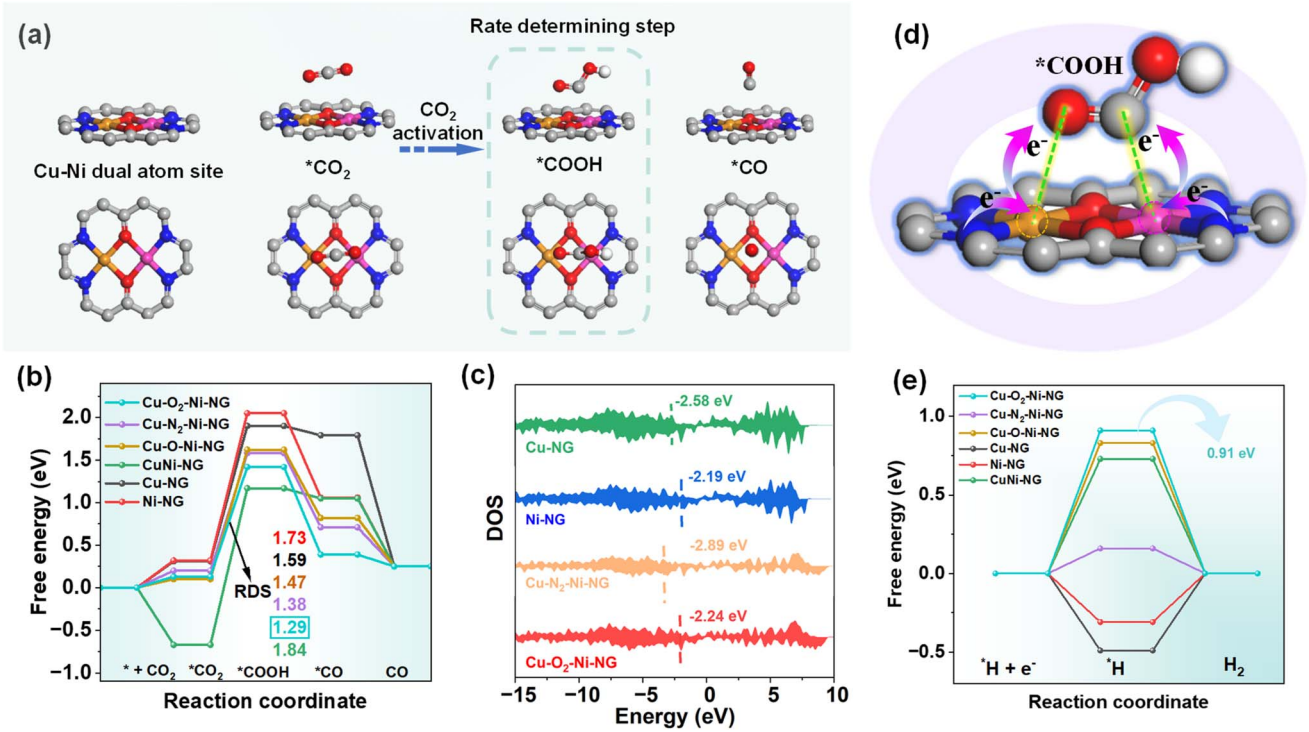

Fig. 5 (a) The stable structure of the Cu–O_2–Ni-NG model and the intermediate structure of the CO_2RR. (b) The free energy diagram of the electroreduction of CO_2 to CO. (c) Density of states plot. (d) The stable structure of the reaction intermediate *COOH of the Cu–O_2–Ni-NG catalyst. (e) Free-energy diagrams for the HER.

(Fig. 5e and Table S7). This larger barrier indicates a suppressed HER pathway, further validating the intrinsic preference of the O-bridged dual-atom configuration for CO_2 reduction.[37]

Conclusions

In summary, this work demonstrates the successful construction of an oxygen-bridged Cu–O_2–Ni-NG dual-atom catalyst anchored on nitrogen-doped graphene through an ultrafast Joule-heating strategy. This approach enables atomically precise immobilization and stable isolation of heteronuclear Cu–Ni pairs, while the unique O-bridge mediates strong electronic coupling between the two metal centers, thereby exerting profound influence on their catalytic behavior. Comprehensive structural analyses and *operando* Raman spectroscopy confirm the formation of well-defined Cu–O_2–Ni-NG motifs and their structural robustness under reaction conditions. Electrochemical evaluation reveals that the Cu–O_2–Ni-NG catalyst delivers significantly enhanced CO_2-to-CO activity, superior selectivity, and excellent operational durability compared with monometallic counterparts. Mechanistic insights obtained from DFT calculations show that the O-bridged geometry optimizes the adsorption kinetics of the key *COOH intermediate, promotes interfacial charge transfer, and tunes the d-band center to an ideal energetic position. These features collectively lower the energy barrier of the RDS while effectively suppressing the competing HER. Overall, this study establishes the oxygen-bridged Cu–Ni dual-atom configuration as a highly efficient and mechanistically distinct platform for CO_2 reduction. More importantly, it underscores the pivotal role of bridge-atom engineering in tailoring the electronic landscape of dual-site catalysts, providing a generalizable design principle for next-generation electrocatalysts aimed at carbon-neutral energy conversion.

Author contributions

Xue Bai: synthesis, experimental measurements, data processing, and writing – original draft. Liyuan Xiao, Xiaoqin Xu, and Anaer Husile: catalyst characterization and testing. Fuquan Bai: theoretical calculations and supervision. Lina Li: synchrotron radiation beamtime and XAS measurements. Jingqi Guan: project supervision, funding acquisition, writing – review & editing.

Conflicts of interest

There are no conflicts to declare.

Data availability

The data supporting this article have been included as part of the supplementary information (SI). Supplementary information is available. See DOI: https://doi.org/10.1039/d6sc01508e.

Acknowledgements

This work was supported by the National Natural Science Foundation of China (No. 92580106 and 22075099) and the Education Department of Jilin Province (No. JJKH20250070BS). The authors acknowledge the BL11B beamline (31124.02.SSRF.BL11B) of the Shanghai Synchrotron Radiation Facility (SSRF) for providing the XAFS beamtime.

Notes and references

1 Y.-F. Tang, L.-B. Liu, M. Yu, S. Liu, P.-F. Sui, W. Sun, X.-Z. Fu, J.-L. Luo and S. Liu, *Chem. Soc. Rev.*, 2024, **53**, 9344–9377.
2 X. Ke, W. Xu, C. Liu, Y. Wang, X. Huang, R. Xiao, X. Xu, T. Li and Z. Shao, *Energy Environ. Sci.*, 2025, **18**, 7792–7858.
3 Y. Duan, W. Ruan and J. Guan, *Coord. Chem. Rev.*, 2025, **543**, 216908.
4 J. Hu, X. Chen, J. Liu and J. Guan, *Chem. Eng. J.*, 2025, **516**, 164199.
5 L.-J. Li, W.-L. Mu, Y.-Q. Tian, W.-D. Yu, L.-Y. Li, J. Yan and C. Liu, *Chem. Sci.*, 2024, **15**, 7643–7650.
6 K. Miao, J. Qin, J. Yang and X. Kang, *Adv. Funct. Mater.*, 2024, **34**, 2316824.
7 L. Lv, R. Lu, J. Zhu, R. Yu, W. Zhang, E. Cui, X. Chen, Y. Dai, L. Cui, J. Li, L. Zhou, W. Chen, Z. Wang and L. Mai, *Angew. Chem., Int. Ed.*, 2023, **62**, e202303117.
8 Q. Hao, H.-x. Zhong, J.-z. Wang, K.-h. Liu, J.-m. Yan, Z.-h. Ren, N. Zhou, X. Zhao, H. Zhang, D.-x. Liu, X. Liu, L.-w. Chen, J. Luo and X.-b. Zhang, *Nat. Synth.*, 2022, **1**, 719–728.
9 Y. Chen, H. Zhu, J. Li, M. Liu, Y. Zhang, Y.-N. Liu and Q. Wang, *Adv. Funct. Mater.*, 2025, **63**, e15847.
10 Z. Chen, H. zhang, Y. Yin, S. Cao, C. Yang, S. Liu, Z. Wang, H. Chen and X. Lu, *Appl. Surf. Sci.*, 2025, **709**, 163804.
11 T. Pu, J. Ding, F. Zhang, K. Wang, N. Cao, E. J. M. Hensen and P. Xie, *Angew. Chem., Int. Ed.*, 2023, **62**, e202305964.
12 X. Huang, X. Li, S. Yan, D. Wang, C. Long, Y. Ying, P. An, Z. Guo, Q. Li, C. Yang, S. Chen, J. Han, L. Chang, S. Lu and Z. Tang, *Sci. Adv.*, 2025, **11**, eads0609.
13 Y. Chen, J. Zhao, X. Pan, L. Li, Z. Yu, X. Wang, T. Ma, S. Lin and J. Lin, *Angew. Chem., Int. Ed.*, 2024, **63**, e202411543.
14 B. Chen, D. Shi, R. Deng, X. Xu, W. Liu, Y. Wei, Z. Liu, S. Zhong, J. Huang and Y. Yu, *ACS Catal.*, 2024, **14**, 16224–16233.
15 J. Zhu, M. Xiao, D. Ren, R. Gao, X. Liu, Z. Zhang, D. Luo, W. Xing, D. Su, A. Yu and Z. Chen, *J. Am. Chem. Soc.*, 2022, **144**, 9661–9671.
16 Z. Sun, C. Li, Z. Wei, F. Zhang, Z. Deng, K. Zhou, Y. Wang, J. Guo, J. Yang, Z. Xiang, P. Ma, H. Zhai, S. Li and W. Chen, *Adv. Mater.*, 2024, **36**, 2404665.
17 Q.-L. Yan, X.-B. Lin, J.-d. Liu, T. Ouyang and Z.-Q. Liu, *Chem. Sci.*, 2026, **17**, 5430–5441.
18 T. Liu, H. Luo, T. Ouyang and Z. Q. Liu, *Adv. Funct. Mater.*, 2024, **35**, 2415367.
19 X. Liu, T. Liu, T. Ouyang, J. Deng and Z. Q. Liu, *Angew. Chem., Int. Ed.*, 2024, **64**, e202419796.
20 X. Bai, T. Tang, J. Sun, F. Bai, J. Hu and J. Guan, *Chin. J. Catal.*, 2026, **80**, 248–257.
21 Y. Tan, J. Huang, H. Lu, T. Chi and J. Sun, *Inorg. Nano-Met. Chem.*, 2019, **50**, 110–113.
22 T. Tang, X. Xu, X. Bai, C. Hou, T. Gan, Z. Wang and J. Guan, *Angew. Chem., Int. Ed.*, 2025, **64**, e202503019.
23 Z. Sun, C. Li, Z. Wei, F. Zhang, Z. Deng, K. Zhou, Y. Wang, J. Guo, J. Yang, Z. Xiang, P. Ma, H. Zhai, S. Li and W. Chen, *Adv. Mater.*, 2024, **36**, e2404665.
24 Y. Zeng, X. Wang, W. Qi, C. Liu, L. Lu, M. Xiao, K. Li, F. Xiao, M. Shao, W. Xing and J. Zhu, *Nat. Commun.*, 2025, **16**, 8111.
25 Q. Li, C. Jia, Q. Wang, X. Guo, K. Qi, J. Liu, W. Fan, L. Luo, J. Li, J. Long, J. Xiao and F. Zhang, *J. Am. Chem. Soc.*, 2025, **147**(43), 39430–39439.
26 M. Liu, Y. Li, L. Yang, P. Zhao, J. Li, L. Tian, D. Cao and Z. Chen, *Angew. Chem., Int. Ed.*, 2025, **64**, e202505268.
27 Y. Yang, W. Zhang, G. Wu, Q. Huang, J. Wen, D. Wang and M. Liu, *Angew Chem. Int. Ed. Engl.*, 2025, **64**, e202504423.
28 J. Jiao, X. Kang, J. Yang, S. Jia, Y. Peng, S. Liu, C. Chen, X. Xing, M. He, H. Wu and B. Han, *J. Am. Chem. Soc.*, 2024, **146**, 15917–15925.
29 X. Bai, T. Tang, X. Bai, S. Zhang, Y. Duan, F. Bai and J. Guan, *Sci. China: Chem.*, 2026, **69**, 953–960.
30 Z. Mei, Y. He, K. Liu, W. Luo, Y. Tan, Q. Chen, H. Wang, X. Guo, Q. Wu, C. Ma, J. Fu, Z. Lin and M. Liu, *J. Am. Chem. Soc.*, 2025, **147**, 34101–34108.
31 M. Wang, H. Chen, M. Wang, J. Wang, Y. Tuo, W. Li, S. Zhou, L. Kong, G. Liu, L. Jiang and G. Wang, *Angew Chem. Int. Ed. Engl.*, 2023, **62**, e202306456.
32 Q. Hao, Q. Tang, L. Zheng, K. Liu, J. Wu and J. Lu, *Nat. Commun.*, 2025, **16**, 8365.
33 M. Yang, Y. Jiang, C.-L. Dong, L. Xu, Y. Huang, S. Leng, Y. Wu, Y. Luo, W. Chen, T. T. T. Nga, S. Wang and Y. Zou, *Nat. Commun.*, 2024, **15**, 9852.
34 F. Wang, X. Han, D. Wu, Z. Wang, X. Xiong, J. Li, X. Gao, G. Wang, L. Huo, Y. Hua, C. Wang, H. Wen, Q. Chen, X. Tian and P. Deng, *Adv. Funct. Mater.*, 2024, **34**, 2314453.
35 L. Zhang, J. Feng, S. Liu, X. Tan, L. Wu, S. Jia, L. Xu, X. Ma, X. Song, J. Ma, X. Sun and B. Han, *Adv. Mater.*, 2023, **35**, e2209590.
36 J. Pei, L. Yang, J. Lin, Z. Zhang, Z. Sun, D. Wang and W. Chen, *Angew Chem. Int. Ed. Engl.*, 2024, **63**, e202316123.
37 Z. Liu, L. Cao, M. Wang, Y. Zhao, M. Hou and Z. Shao, *J. Mater. Chem. A*, 2024, **12**, 8331–8339.